LES of hypersonic compression-corner flows with upstream sub-boundary-layer microramp vortex generators

By J. Kim, I. Bermejo-Moreno†, A.-M. Schreyer‡ AND J. Urzay

1. Motivation and objectives

The inclusion of microramps upstream of the interaction between shock waves and turbulent boundary layers has been experimentally proven as an effective technique to passively control shock-induced boundary-layer separation (Barter & Dolling 1995; Anderson *et al.* 2006; Babinsky *et al.* 2009; Schreyer *et al.* 2011a). To minimize performance penalties, for instance in the form of increased drag, the microramps are fully immersed in the boundary layer, but partially protrude above the viscous sublayer. The primary control mechanism is attributed to the pair of counter-rotating vortices produced at each side of the symmetric, triangularly shaped microramps. These vortices coherently propagate downstream of the generating microramp and away from the wall, thus enabling the wall-normal exchange of streamwise momentum between high- and low-speed regions of the boundary layer. As a consequence, the boundary layer is strengthened in a way that it can better resist the adverse pressure gradients imposed by the downstream interaction with the shock that otherwise leads to separation. Because of the interplay between low-frequency unsteadiness of the separation bubble and shock system (Clemens & Narayanaswamy 2014), the reduction of the separation region made possible by the microramps also has a stabilizing effect on the shock dynamics (Ford & Babinsky 2007).

The present study focuses on large-eddy simulations (LES) of the set-up studied experimentally by Schreyer *et al.* (2011b) to assess the effect of a two-row layout of the microramps on a compression ramp-induced shock interacting with a hypersonic (Mach number M= 7.2) turbulent boundary layer. The majority of previous experimental and numerical studies on the microramps has focused on interactions at much lower Mach numbers.

A preliminary numerical study of the experimental configuration considered in this report was carried out as part of the CTR 2016 Summer Program (Schreyer *et al.* 2016) in a reduced-size domain. In that earlier study, the effect of the microramps was introduced as a modified inflow condition to the computational domain to avoid the added geometric meshing complexity. The simulations presented in this report address a larger computational domain that includes the microramps. The results improve the fidelity of our prior simulations in Schreyer *et al.* (2016) and reproduce more accurately the experimental configuration.

The remainder of this report is organized as follows: Section 2 describes the computational set-up for the numerical simulations performed in this study. Results of two sets of simulations are presented in Sections 3.1 and 3.2 for the baseline and controlled configurations, respectively. Conclusions are provided in Section 4.

† Aerospace and Mechanical Engineering Department, University of Southern California
‡ Technical University of Braunschweig, Germany

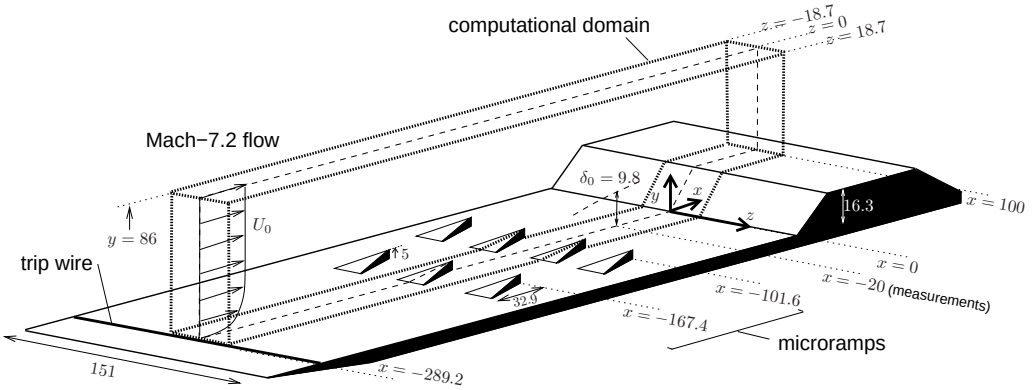

FIGURE 1. Schematics of the full experimental geometry and the LES computational domain. Dimensions are in mm.

2. Computational set-up

The LES performed in this study refer to the same geometry and flow conditions as in the experiments described in Schreyer *et al.* (2011a,b). The experimental geometry along with the corresponding computational domain are sketched in Figure 1. The computational domain occupies only a portion of the full configuration. The inflow and outflow planes are located, respectively, at $x = -289.25$ mm and $x = 100$ mm relative to the corner location $x = 0$. The height of the domain is $y = 86$ mm relative to the upstream surface of the flat plate $y = 0$. The domain is truncated in the spanwise direction at $z = \pm 18.75$ mm to reduce computational cost, which gives a spanwise domain size of $3.8\delta_0$, where $\delta_0 = 9.8$ mm is the experimentally-measured boundary-layer thickness 20 mm upstream of the ramp corner. Two cases are addressed in the computations: a baseline case in which the microramps are removed and the flow becomes a compression-corner flow (see Figure 2a), and a controlled case with the microramps in which the first row supports one entire vortex generator while the second row contains two separate halves (see Figure 2b). Note that the present simulations extend previous work by Schreyer *et al.* (2016) where the effect of the microramps was modeled as a modified inflow boundary condition in a smaller computational domain.

The compressible LES conservation equations are solved using the in-house CTR unstructured code CharLES (Khalighi *et al.* 2011). The filtered conservation equations are discretized in space using a cell-based finite-volume formulation of fourth-order accuracy in uniform Cartesian grids and second-order accuracy in arbitrary unstructured meshes. An essentially non-oscillatory (ENO) shock-capturing scheme is applied near shock waves. Time advancement is done using a standard third-order Runge-Kutta method. The subgrid-scale (SGS) model of Vreman (2004) is used for the unclosed fluxes of momentum and energy with a model constant equal to 0.07 and a constant turbulent Prandtl number equal to 0.9. The air flow is assumed to be that of a calorically perfect gas with an adiabatic coefficient equal to 1.4. The molecular viscosity is assumed to be a function of temperature powered to 0.76, with a constant Prandtl number equal to 0.7.

Synthetic turbulence is generated at the inflow boundary $x = -289.25$ mm using the digital filtering technique of Touber & Sandham (2009), which requires inputs in terms of Reynolds stresses and mean velocities. The wall-normal profiles of those quantities were measured using PIV at a plane located at $x = -20$ mm in the baseline configuration

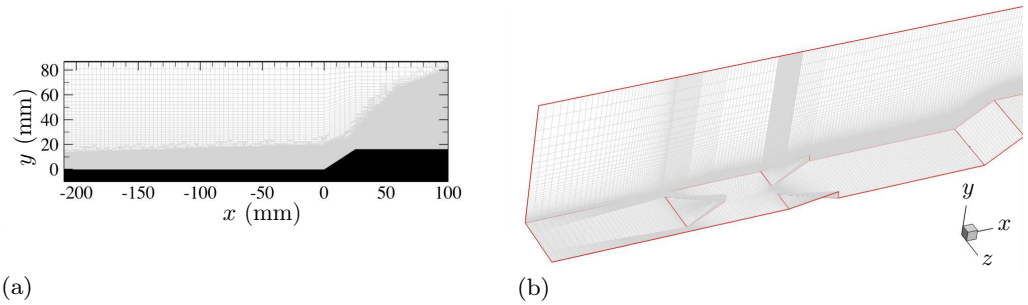

(a) (b)

FIGURE 2. Computational grids for (a) the baseline case at $z = 0$ (after grid adaption) and (b) the controlled case at $z = -18.75$ mm and $y = 0$ (before grid adaption).

(Schreyer *et al.* 2011a,b). In the simulations, the experimental profiles are rescaled and imposed as an inflow boundary condition such that they are recovered in the baseline case at the measurement station $x = -20$ mm. The pressure is assumed uniform on the inflow plane and equal to the wall pressure value 1366 Pa measured experimentally. The mean temperature profile in the wall-normal direction is also imposed by the experimental measurement. For the synthetic turbulence, the integral length scale (characterizing two-point correlations) is taken as $\delta_0 = 9.8$ mm, and the integral time scale is of order δ_0/U_0, with $U_0 = 1146$ m/s the free-stream velocity. Turbulence statistics at $x = -20$ mm were not sensitive to the choice of δ_0 and U_0. An absorbing buffer zone is used at the outflow boundary condition. No-slip boundary conditions are used on walls, where the temperature is kept constant at 340 K, the same as the experimental wall temperature. A slip boundary condition is applied on the top boundary. Spanwise periodicity is employed on the side boundaries.

Cross sections of the computational grids are shown in Figure 2 for the baseline and controlled cases, the latter being shown before any mesh adaption. For the baseline simulation, the minimum grid spacings are $\Delta y^+ = 3$, $\Delta x^+ = 22$, and $\Delta z^+ = 22$ in wall viscous units. In outer units, the first grid point is located at $y \sim 0.01\delta_0$ away from the wall. The controlled case requires finer grid resolution than the baseline one due to the added geometrical complexity of the leading edges of the microramps. The total number of computational cells is 3.6 million for the baseline simulation and 5.8 million for the controlled case, respectively. The current simulations do not strictly qualify as wall-resolved LES, for which additional grid refinement would be required in the wall-normal direction so as to make $\Delta y^+ \approx 1$ (Larsson *et al.* 2016).

The integration time for the baseline case is 12.7 ms, and the controlled one is 6.6 ms; these correspond, respectively, to 36 and 19 flow-through times. The time-step size is $\Delta t = 7 \times 10^{-8}$ s for the baseline case and 1.2×10^{-8} s for the controlled case, in such a way that the resulting CFL numbers are approximately unity for both cases.

3. Numerical results

The description of the numerical results is subdivided into a section where the results of the baseline simulation are compared with the PIV measurements of Schreyer *et al.* (2011b), followed by an analysis of the effect of the microramps on the controlled configuration. When indicated, averaging is performed in time and along the spanwise direction in the baseline flow, whereas the controlled configuration is amenable to only time averaging due to the flow inhomogeneity in the spanwise direction.

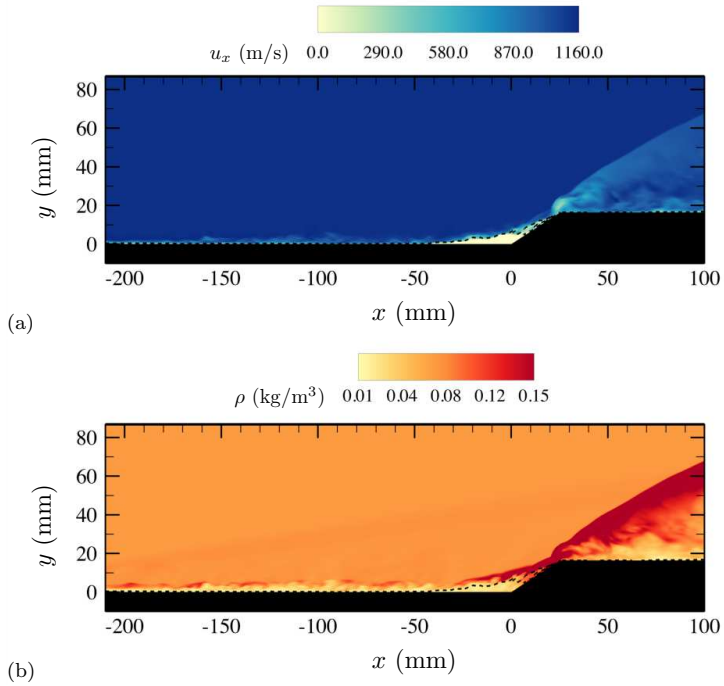

FIGURE 3. Instantaneous contours of (a) streamwise velocity and (b) density at the spanwise centerplane. The dotted lines indicates the sonic line.

3.1. *Baseline configuration (without the microramps)*

Figure 3 shows instantaneous contours of streamwise velocity and density at the $z = 0$ plane. The interaction of the incoming boundary layer with the positive pressure gradient generated at the compression corner causes flow separation and a recirculation bubble in that region. As a result, a classic separation shock is formed upstream of the corner. The separation shock intersects a reattachment shock downstream near the top of the ramp. The reattachment shock is visible in the contours as a density discontinuity that emerges near the upper end of the compression ramp. Note that a flow field similar to the one calculated here has been qualitatively observed in the experiments using surface-flow visualizations (Schreyer *et al.* 2011b).

A quantification of the similarities between experimental and numerical results is shown in Figures 4-5. Specifically, Figure 4(a) shows a comparison of time- and spanwise line-averaged streamwise velocity profiles in the wall-normal direction at several streamwise locations. Overall, good agreement with the PIV measurements is observed for $y/\delta_0 \gtrsim 0.2$. A recirculation zone having negative streamwise velocities occurs near the wall in the mean velocity profiles for all the streamwise locations reported in Figure 4(a). Although this recirculation zone, which is responsible for the separation shock, is not clearly detected in the PIV measurements, it is recognized that the latter have limitations in describing the flow near the corner (Schreyer *et al.* 2016). The LES results in the present investigation improve those in Schreyer *et al.* (2016), in that the numerical velocity profiles display better agreement with the experimental results everywhere. However, larger discrepancies are observed for the root-mean-square (rms) streamwise velocities in Fig-

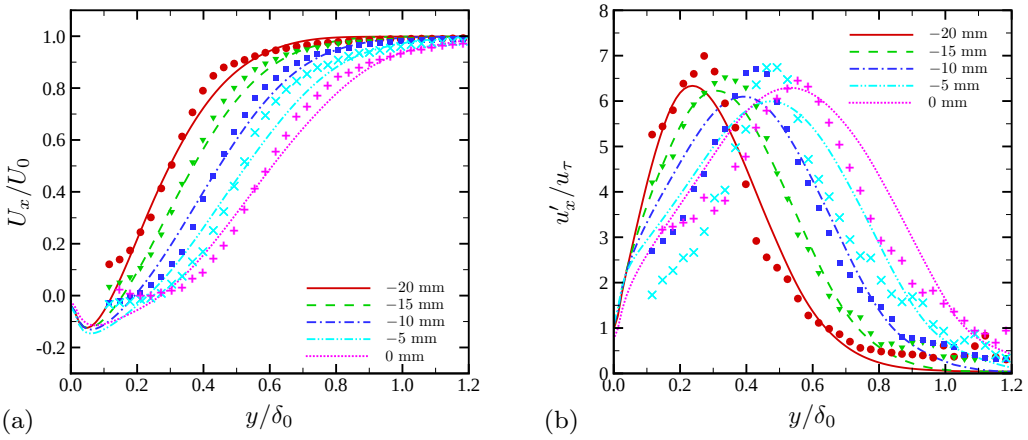

FIGURE 4. Comparisons of (a) averaged streamwise velocity and (b) rms of streamwise velocity fluctuation between LES (lines) and PIV (symbols) at several streamwise locations upstream of the compression ramp: solid line and circle, $x = -20$ mm; dashed line and triangle, $x = -15$ mm; dashed-dot line and square, $x = -10$ mm; dashed-dot-dot line and diagonal cross, $x = -5$ mm; dotted line and plus, $x = 0$ mm. The free-stream velocity $U_0 = 1146$ m/s and the friction velocity $u_\tau = 57.3$ m/s at $x = -20$ mm are used, coincident with the experimental values.

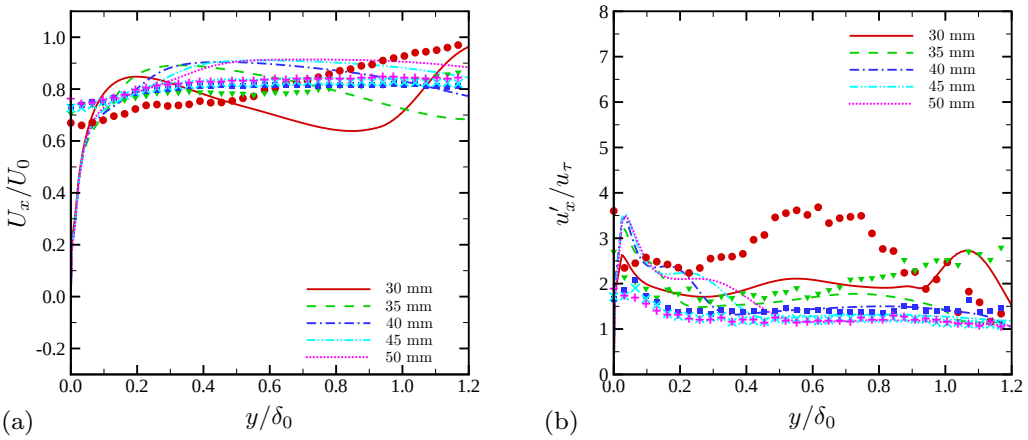

FIGURE 5. Comparisons of (a) averaged streamwise velocity and (b) rms of streamwise velocity fluctuation between LES (lines) and PIV (symbols) at several streamwise locations downstream of the expansion corner: solid line and circle, $x = 30$ mm; dashed line and triangle, $x = 35$ mm; dashed-dot line and square, $x = 40$ mm; dashed-dot-dot line and diagonal cross, $x = 45$ mm; dotted line and plus, $x = 50$ mm. Refer to caption in Figure 4 for normalization quantities.

ure 4(b), and for similar quantities evaluated downstream of the compression corner in Figure 5. These discrepancies, which suggest deficiencies in some aspects of the LES near-wall resolution or in the subgrid-scale models employed here, will be examined more closely in future research.

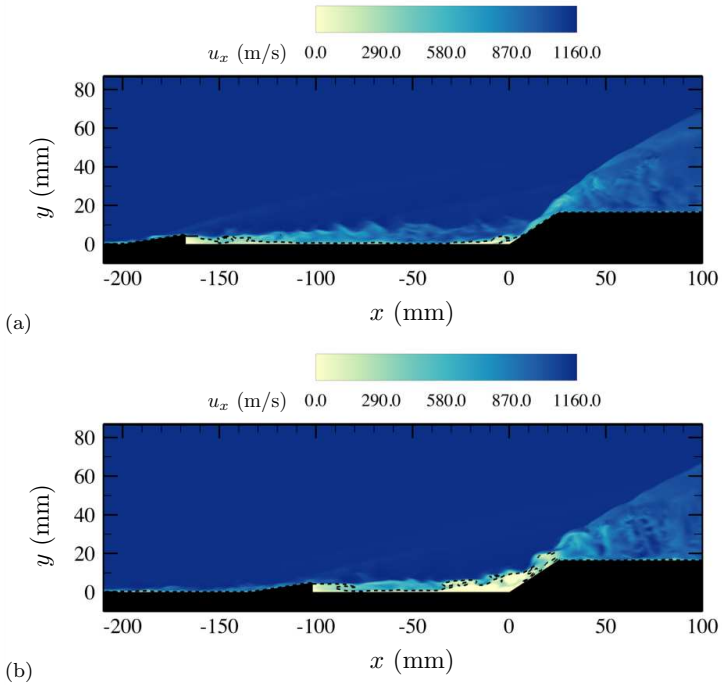

FIGURE 6. Instantaneous contours of streamwise velocity at (a) $z = 0$ and (b) $z = 18.75$ mm. The dotted lines indicate a sonic line where the local Mach number is unity.

3.2. *Controlled configuration (with the microramps)*

The effect of placing the microramps upstream of the compression corner is qualitatively visualized in the instantaneous contours of streamwise velocity shown in Figure 6 at two spanwise locations. In particular, the locations correspond to $z = 0$ (spanwise centerplane) and $z = 18.7$ mm (side boundary plane), which coincide with the symmetry planes of the microramps located on the front and second rows, respectively (see Figure 1). In principle, the size of the recirculation bubble is different on each spanwise plane depending on the distance from the compression corner to the aft of the microramp where the wake is generated. Specifically, a short recirculation bubble is observed in the visualizations along the centerplane in Figure 6(a), corresponding to the case where the microramp aft is farthest from the corner, whereas the opposite holds in Figure 6(b). Further observations of this phenomenon, in an averaged sense, are made in Figure 7. In particular, Figure 7(c) shows a statistical reduction of the size of the recirculation bubble on the centerplane with respect to the baseline case in Figure 7(a), with the opposite trend being observed on the side boundary plane provided in Figure 7(c).

Figures 6-7 suggest that the distance from the microramp aft to the compression corner is an important factor. However, the three-dimensional visualizations in Figure 8 indicate that the strength of the wake educed from the leading microramp has largely decreased upstream of the corner (see Figure 8c). In comparison, the counter-rotating pair of vortices in the wakes educed from two microramps closest to the corner are much more intense near the recirculation bubble, as observed in the transverse isocontours in Figure 8(c), thereby creating a synergistic down-washing motion in the boundary

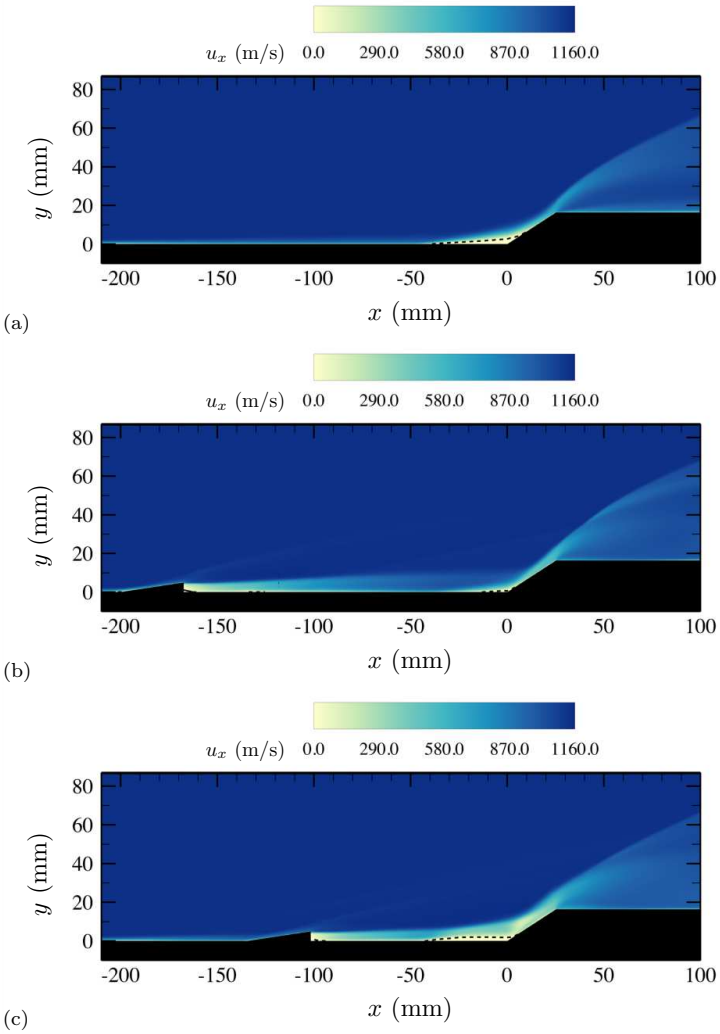

FIGURE 7. Time-averaged contours of streamwise velocity for (a) the baseline uncontrolled configuration (spanwise-averaged), (b) the controlled case at $z = 0$, and (c) the controlled case at $z = 18.75$ mm. The dotted lines correspond to zero-velocity contours.

layer near the centerline whose effect may be to hinder early separation in that zone. Nonetheless, the precise mechanism of alteration of the recirculation bubble by the educed wakes is unclear from these visualizations, and further analyses are required. Additionally, the strong spanwise variation of the control effects suggests that the present staggered arrangement of the microramps can be optimized to further suppress the separated flows.

The strong velocity disturbances introduced by the microramps in the boundary layer with respect to the baseline case are highlighted in Figure 8(a,b). These provide an important obstacle in undertaking computations in reduced-size versions of the computational domain, as in our earlier study (Schreyer *et al.* 2016). Specifically, the middle transverse panel in Figure 8(c) corresponds to the inflow location used in Schreyer *et al.* (2016) where a synthetic inflow boundary condition is manufactured in order to model

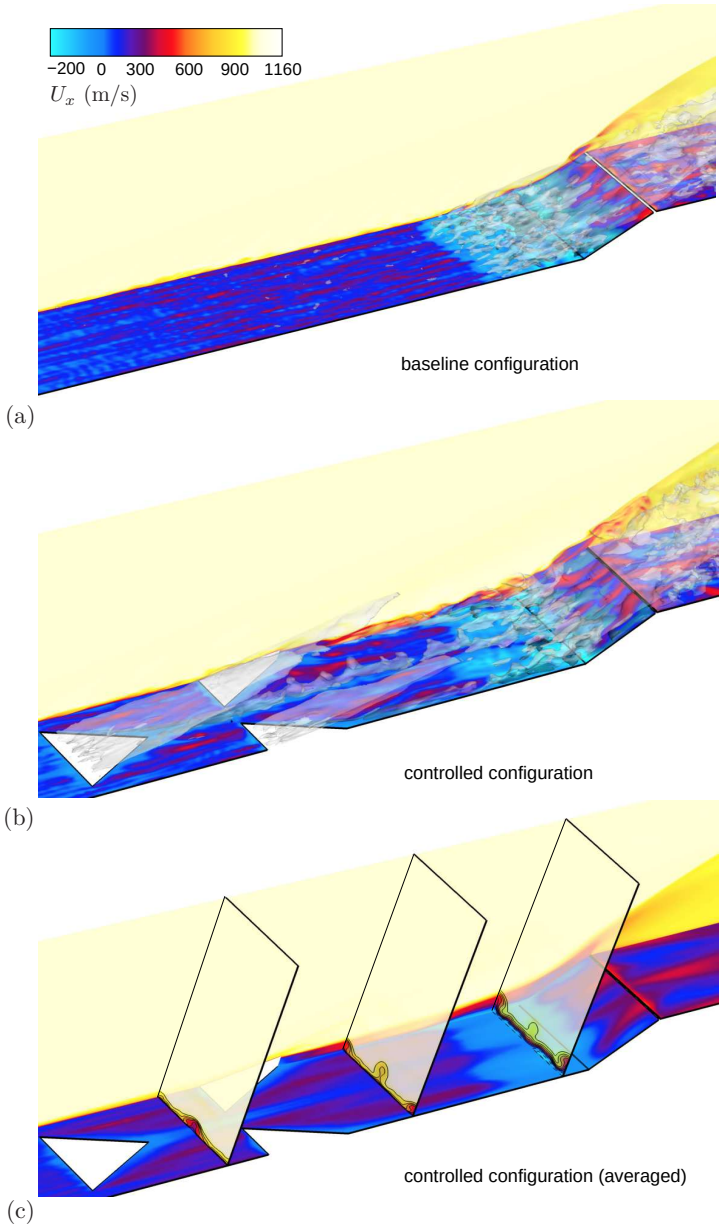

FIGURE 8. Isocontours of streamwise velocity for (a) instantaneous baseline configuration, (b) instantaneous controlled configuration, and (c) time-averaged controlled configuration. In panels (a,b), isosurfaces of wall-normal velocity equal to 95 m/s are indicated by gray color. All horizontal planes are located 0.1 mm above the wall. In panel (c), the three streamwise normal planes correspond to $x = -150$, -75, and -11 mm, respectively.

the effects of the microramps. Although Figure 8(c) resembles Figure 3 of Schreyer *et al.* (2016), including the Λ-type footprints on the compression ramp, the utilization of a larger domain in this study makes unnecessary a synthetic inflow boundary condition in

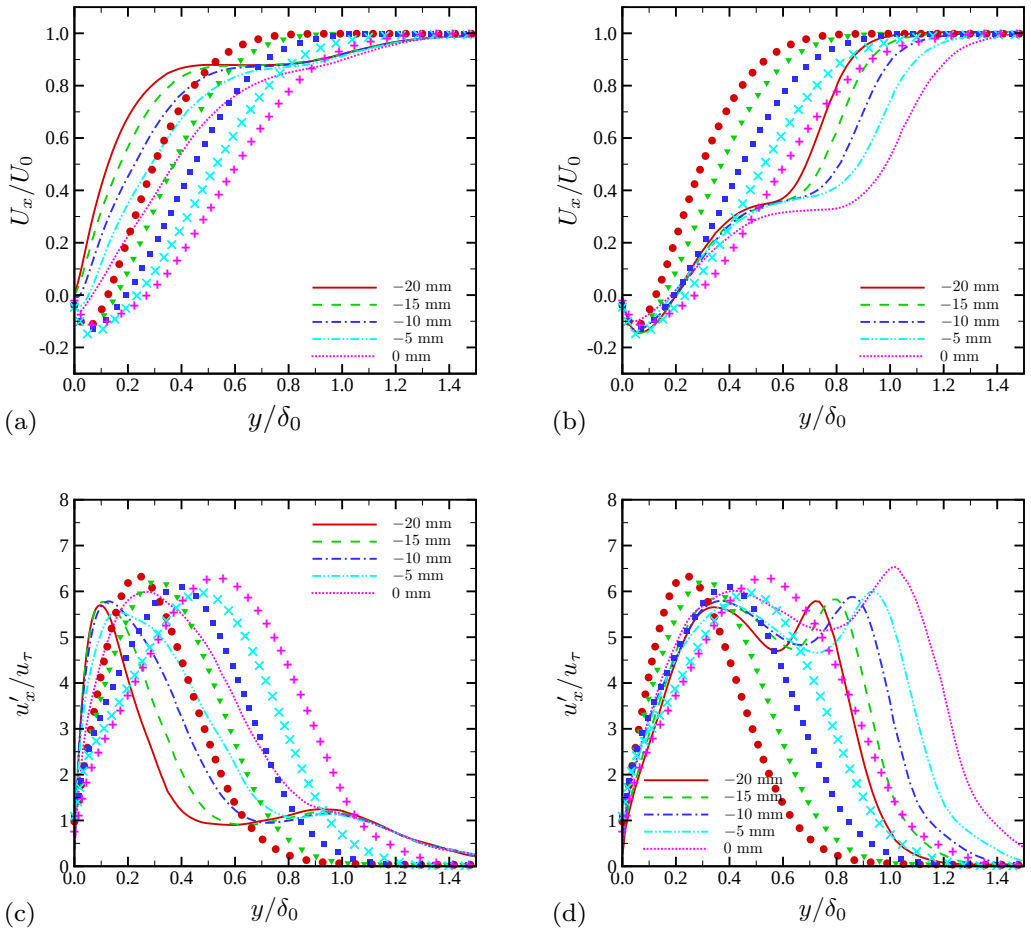

FIGURE 9. Averaged streamwise velocity profiles in the wall-normal direction at (a) $z = 0$ and (b) $z = 18.75$ mm, and streamwise velocity fluctuation rms profiles in the wall-normal direction at (c) $z = 0$ and (d) $z = 18.75$ mm. Lines correspond to the controlled case, and symbols denote the results of the baseline uncontrolled configuration (as plotted in Figure 4a and b): solid line and circle, $x = -20$ mm; dashed line and triangle, $x = -15$ mm; dashed-dot line and square, $x = -10$ mm; dashed-dot-dot line and diagonal cross, $x = -5$ mm; dotted line and plus, $x = 0$ mm. The free-stream velocity $U_0 = 1146$ m/s and the friction velocity $u_\tau = 57.3$ m/s at $x = -20$ mm are used, coincident with the experimental values.

the wake of the microramps and, as a consequence, results in improved comparisons with experiments.

A comparison between baseline (symbols) and controlled (lines) profiles of time-averaged streawise velocity is provided in Figure 9 on the two spanwise planes reported in Figures 6-7. On approach to the corner along the centerplane $z = 0$, the turbulent boundary layer in the controlled case is more attached and the separation region is nearly suppressed, as evidenced in Figure 9(a) by the reduction in the magnitude of the negative values of streamwise velocity. Conversely, on approach to the corner along the side boundary plane $z = 18.75$ mm, the disturbances created by the microramp located closest to the corner noticeably modify the baseline profiles. As a result, the size of the recircula-

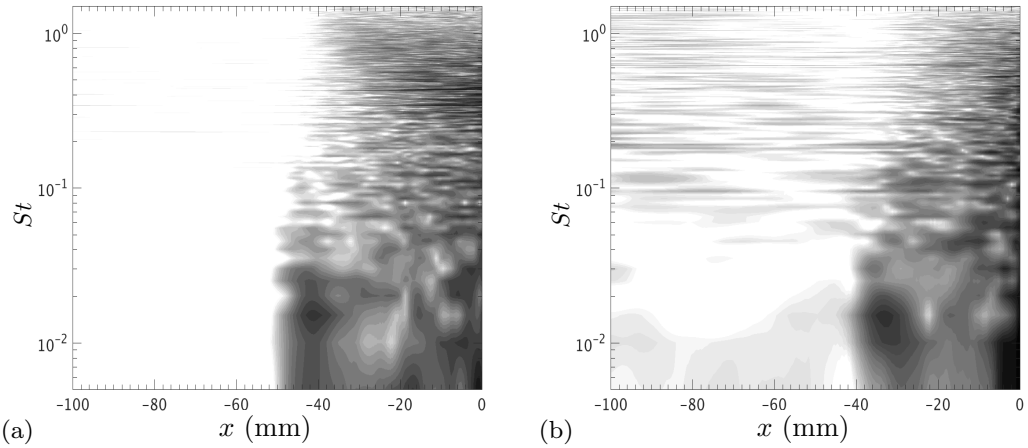

FIGURE 10. Contours of power-spectral density of wall-pressure fluctuations on the $z = 0$ mm plane for (a) the baseline and (b) controlled configurations. The average recirculation zone starts at $x \approx -40$ mm (see also Figure 7).

tion zone becomes larger, and additional inflection points appear, presumably due to the wake deficit. These are accompanied with double-peak shapes in the wall-normal profiles of rms streamwise velocity.

Turbulent boundary-layer separation induced by shock-wave interactions often involves the low-frequency oscillations of separation shock, especially in its immediate upstream region (Clemens & Narayanaswamy 2014). The characteristic frequency of such unsteadiness is one or two orders of magnitude smaller (~ 0.01 to $0.1U_0/\delta_0$) than those of incoming turbulent boundary layers ($\sim U_0/\delta_0$). The root cause of the low-frequency shock oscillations is not completely explained, though recent studies have provided important clues to understanding this phenomenon (Clemens & Narayanaswamy 2014; Sandham 2016). To investigate the oscillation dynamics in the present configuration, Figure 10 provides the power-spectral density (PSD) of wall-pressure fluctuations as a function of the streamwise location and non-dimensional frequency $\mathrm{St} = f\delta_0/U_0$. The PSD is computed using Welch's method, with 50% overlapping window following Priebe & Martin (2012). At $x \approx -40$ mm, just upstream of the separation bubble, low-frequency oscillations are clearly seen for $\mathrm{St} \lesssim 0.03$, and the streamwise location of these oscillations is slightly delayed downstream by 5 to 10 mm in the controlled case. In all cases, the pressure oscillations caused by the incoming turbulent boundary layer are much smaller compared to those resulting from the interaction.

A closer examination of the wall-pressure PSD at three streamwise locations upstream of the ramp corner is illustrated in Figure 11. At $x = -60$ mm, both cases have broadbanded peaks around $\mathrm{St} \approx 0.6$, comparable to the outer-scale frequency of the incoming turbulent boundary layer. The controlled flow contains an additional broadbanded peak around $\mathrm{St} \approx 0.01$ due to the trailing vortices shed from the microramps. As shown in Figure 10(b), the effects of the microramps shift the low-frequency spectral peak by 5 to 10 mm downstream. With the shift taken into account, Figure 11(b) shows the PSD of the baseline and controlled cases at $x = -40$ mm and -33 mm, respectively. The low-frequency peaks and the amplitudes agree well, which suggests that both flows have similar low-frequency oscillations of the separation shock. This observation is in-

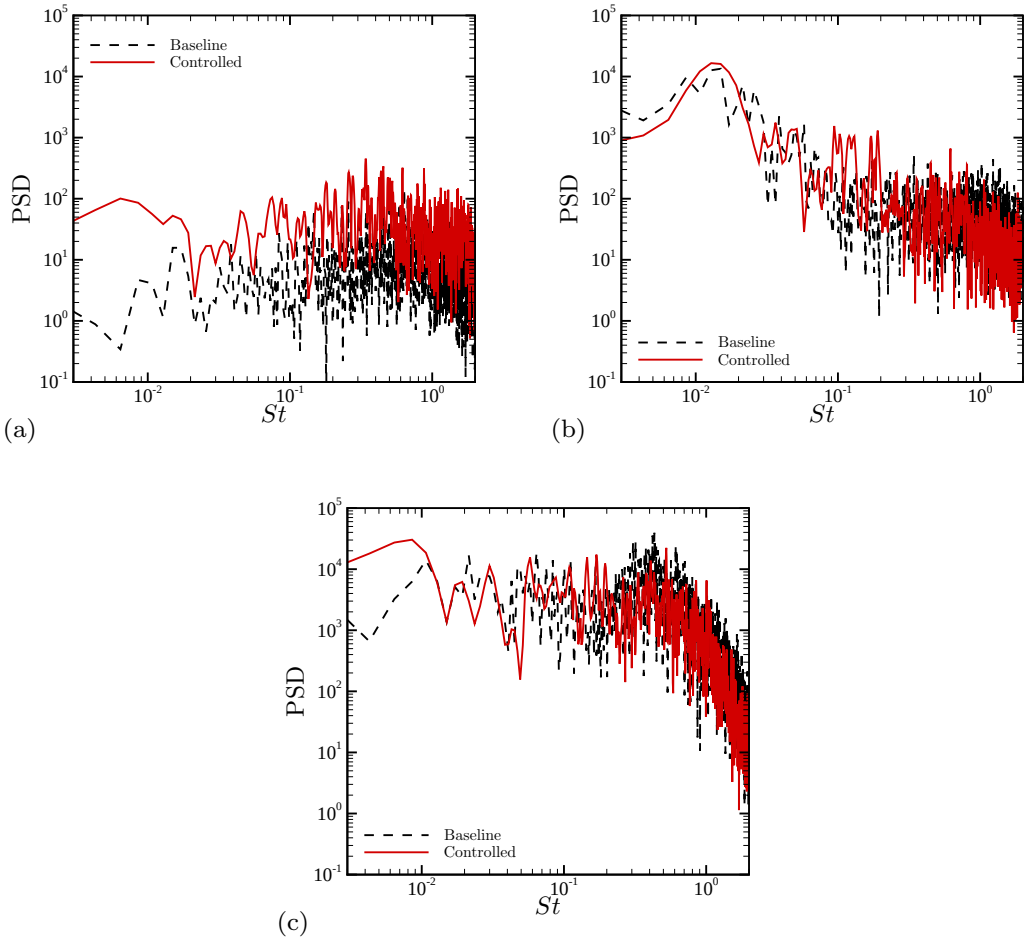

FIGURE 11. The centerplane ($z = 0$) PSD of wall-pressure fluctuations at (a) $x = -60$ mm, (b) $x = -40$ mm (baseline) and -33 mm (controlled), and (c) $x = -5$ mm.

teresting because the incoming boundary layers of the two flows are characterized by large differences in fluctuation amplitude at St $\lesssim 0.03$, although they exhibit very similar low-frequency oscillations in the intermittent region. Further downstream near the compression corner, the two spectra become similar, as shown in Figure 11(c).

In Figure 12, the streamwise variation of PSD of wall-pressure fluctuations at St $= 0.014$ is shown, corresponding to the low-frequency peak in Figure 11(b). In both cases, fluctuations at St $= 0.014$ grow exponentially in the range -45 mm $\lesssim x \lesssim -30$ mm. The spatial growth rate is shown in Figure 12, which suggests that the upstream mechanism inducing the low-frequency unsteadiness results may be linear. Their spectral peaks coincide with the streamwise location where the separation bubble begins to form. For example, in Figure 12(a), the spectral peak of the controlled flow is located further downstream, which is consistent with the smaller separated zone shown in Figure 7(b). An interesting effect of the microramps is that they render the low-frequency oscillations more correlated in the spanwise direction in such a way that the growth rate and

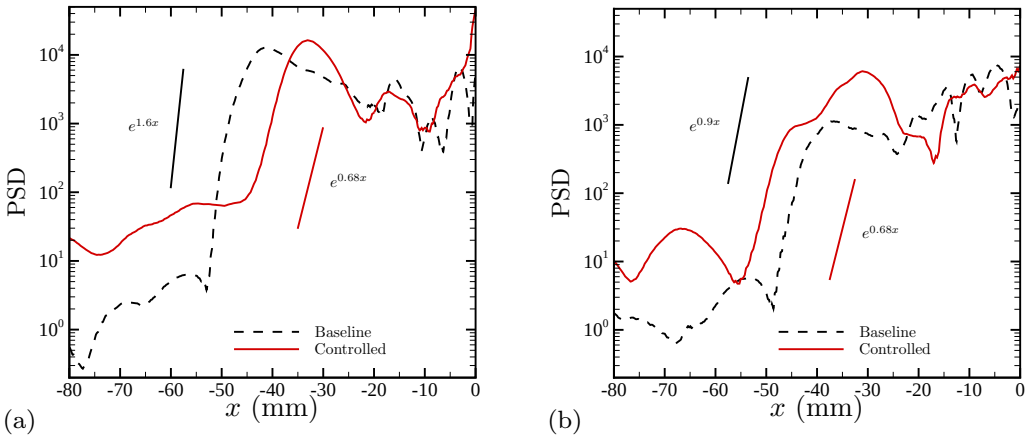

FIGURE 12. Streamwise profiles of wall-pressure PSD at St = 0.014 on the (a) centerplane $z = 0$ and (b) side boundary plane $z = 18.75$ mm.

spectral peak amplitude are insensitive to changes in spanwise position. Because of the strong modulation generated by the microramps, the locations of the shock foot vary significantly in the spanwise direction.

4. Conclusions

In this study, the interaction of sub-boundary-layer microramp vortex generators with a hypersonic Mach-7.2 flow over a 33° compression ramp has been investigated using LES. The simulations reproduce the experimental configuration studied by Schreyer *et al.* (2011a,b). As an extension of our previous work (Schreyer *et al.* 2016), the full geometry of the microramp vortex generators in two staggered rows is included in the computational domain, and their effects on the flow near the compression corner are characterized. This extension proves to be beneficial in that the qualtitative structure of the flow and the mean streamwise velocity profiles show improved agreement with experimental measurements. The microramps are found to have drastically different control effects, depending on the spanwise location along the ramp. For instance, on approaching the corner on the symmetry plane of the leading microramp, the separated zone is significantly reduced in size, whereas the opposite holds on the symmetry planes of the microramps located closest to the corner. On average, the microramps displace downstream the low-frequency unsteadiness of the interaction zone. However, the maximum spectral amplitude of the wall-pressure fluctuations is nearly the same with or without the microramps. Future work may involve additional grid refinement, statistical convergence, wall modeling, and global stability analyses of the mean flow to gain insight into the underlying control mechanisms of optimized microramp configurations.

Acknowledgments

This work was funded by US AFOSR, Grant #1194592-1-TAAHO. The first author is grateful to Prof. Sang Lee (University of New Mexico) for useful discussions on the grid generation for the microramps.

REFERENCES

Anderson, B. H., Tinapple, J. & Surber, L. 2006 Optimal control of shock wave turbulent boundary layer interactions using micro-array actuation. *AIAA Paper* 2006-3197.

Babinsky, H., Li, Y., & Ford, C. W. P. 2009 Microramp control of supersonic oblique shock-wave/boundary-layer interactions. *AIAA J.* **47**, 668–675.

Barter, J. W. & Dolling, D. S. 2009 Reduction of fluctuating pressure loads in shock/boundary-layer interactions using vortex generators. *AIAA J.* **33**, 1842–1849.

Bermejo-Moreno, I., Larsson, J. & Lele, S. K. 2010 LES of canonical shock-turbulence interaction. *Annual Research Briefs*, Center for Turbulence Research, Stanford University, pp. 209–222.

Clemens, T. & Narayanaswamy, V. 2014 Low-frequency unsteadiness of shock wave/turbulent boundary layer interactions. *Annu. Rev. Fluid Mech.* **46**, 469–492.

Dupont, P., Haddad, C. & Debieve, J.-F. 2006 Space and time organization in a shock-induced separated boundary layer. *J. Fluid Mech.* **559**, 255–277.

Ford, C. W. P. & Babinsky, H. 2007 Micro-ramp control for oblique shock wave/boundary layer interactions. *AIAA Paper* 2007-4115.

Khalighi, Y., Nichols, J. W., Lele, S. K., Ham, F. & Moin, P. 2011 Unstructured large eddy simulation for prediction of noise issued from turbulent jets in various configurations. *AIAA Paper* 2011–2886.

Larsson, J., Kawai, S., Bodart, J. & Bermejo-Moreno, I. 2016 Large eddy simulation with modeled wall-stress: Recent progress and future directions. *Mech. Eng. Rev.* **3**, 15-00418.

Lee, S. 2009 *Simulation of shock boundary layer interaction control using micro-vortex generators.* Ph.D. thesis, University of Illinois at Urbana-Champaign, USA.

Priebe, S. & Martin, M. P. 2012 Low-frequency unsteadiness in shock wave-turbulent boundary layer interaction. *J. Fluid Mech.* **699**, 1–49.

Sandham, N. 2016 Effects of compressibility and shock-wave interactions on turbulentshear flow. *Flow Turbul. Combust.* **97**, 1–25.

Schreyer, A.-M., Sahoo, D. & Smits, A. J. 2011 Experiments on the influence of a microramp array on a hypersonic shock turbulent boundary layer interaction. *AIAA Paper* 2011-3428.

Schreyer, A.-M., Sahoo, D. & Smits, A. J. 2011 Turbulence measurements with PIV in a hypersonic shock/boundary layer interaction. *AIAA Paper* 2011-3429.

Schreyer, A.-M., Bermejo-Moreno, I., Kim, J. & Urzay, J. 2016 Separation control in a hypersonic compression ramp interaction. *Proceedings of the Summer Program*, Center for Turbulence Research, Stanford University, pp. 223–232.

Touber, E. & Sandham, N. 2009 LES of low-frequency unsteadiness in a turbulent shock-induced separation bubble. *Theor. Comput. Fluid Dyn.* **23**, 79–107.

Vreman, A. W. 2004 An eddy-viscosity subgrid-scale model for turbulent shear flow: Algebraic theory and applications. *Phys. Fluids* **16**, 3670–3681.